IEEE Access
Multidisciplinary ⋮ Rapid Review ⋮ Open Access Journal

Received April 9, 2019, accepted April 22, 2019, date of publication May 1, 2019, date of current version May 15, 2019.

Digital Object Identifier 10.1109/ACCESS.2019.2914346

Hardware-in-the-Loop Framework for Validation of Ancillary Service in Microgrids: Feasibility, Problems and Improvement

YUJIA HUO, (Student Member, IEEE), AND GIAMBATTISTA GRUOSSO, (Senior Member, IEEE)
DEIB, Politecnico di Milano, 20133 Milan, Italy

Corresponding author: Giambattista Gruosso (giambattista.gruosso@polimi.it)

ABSTRACT Testing complex micro-networks requires the availability of specialized laboratories and interconnected devices. This paper describes the development of a controller-hardware-in-the-loop simulation in the context of the microgrid. This approach provides genuine testing and debugging environment for converter controllers in microgrid under various test conditions by means of real-time simulation. It is also viable to test microgrid dispatching strategies. The platform structure and real-time simulation issues including modeling, circuit partition, and multi-rate design are studied, demonstrating the rationality, and transferability of the design scheme. In the interest of studying the integration of distributed energy resources, a novel low-level control method, which enables the power converters to function as both grid-supplying and grid-supporting, is tested. Some practical implementation issues of the theoretical control algorithm are exposed and alleviated, which shows the value of hardware-in-the-loop simulation, and at the same time contributes evidence to modifying theoretical algorithms in industrial applications.

INDEX TERMS Ancillary service, distributed energy resources, hardware-in-the-loop, microgrid.

I. INTRODUCTION

Distributed Energy Resources (DERs), popularly referring to Renewable Energy Resources (RESs) and Electrical Energy Storage (EES), are of interest to many countries nowadays, as they are foreseen to be promising participants in the evolution of power systems. DERs have been integrated mostly as supplementary generation but on the other hand, are castigated for lacking natural inertia, for the low controllability in terms of distribution system, and for the unpredictable yield of RESs. This not only challenges the reliability of the network, also results in a passive distribution grid with overrated installed capacity. Numerous studies are conducted on grid-tied converters to mitigate the adverse effects by deploying the high controllability of power electronics, reinforcing DERs' roles of grid-feeding [1], grid-supporting [2]–[4] and even grid-forming [5], [6]. Therefore, advanced simulation methods are called for and co-simulations supported by Controller Hardware-In-the-Loop (C-HIL) technique stand out, responding to the demand for DER integration study [7]–[10]. HIL is industrially significant. It avoids crashing the costly part of the system and guarantees safety and at the same time, it offers a large coverage of test conditions and traceable replicas of the same tests [11], [12]. More importantly, it is independent from the long-term waiting of the construction of real The main purpose of this article is to offer a guided methodology for the realization of a hardware in the loop system aimed at the development of the control algorithm. As an example, we consider a micro-network consisting of a synchronous generator and a PV, in which we want to study a simple algorithm for frequency control. This approach, although simplified, allows to highlight the problems and the methodological solutions necessary for the correct implementation of the problem. This in different scales is one of the most interesting and challenging aspects of the microgrids landscape [6].

The work starts from the idea of creating a generalized framework for the simulation of electrical systems. This framework has already been presented by the authors previously [13], although it is limited to the photovoltaic part only. In this work we want to focus on the integration of DERs from the point of view of algorithms developed by digital controllers. Meanwhile, the concept of a platform for C-HIL co-simulation in the microgrid is extended.

The associate editor coordinating the review of this manuscript and approving it for publication was Fabrizio Messina.

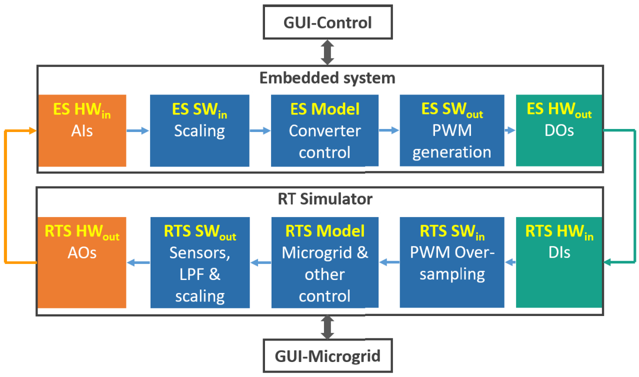

FIGURE 1. Functional diagram of the proposed C-HIL framework.

TABLE 1. Signal list for RTS.

signal	range	physical range	REZ	f_s	I/O
$V_{a,b,c}$	± 10 V	± 1000 V	30.5 mV	50 kHz	AO
$I_{a,b,c}$	± 10 V	± 1000 A	30.5 mA	50 kHz	AO
$S_{a,b,c}$	5V-TTL	non-inverting	20 ns	50 MHz	DI

TABLE 2. Signal list for ES.

signal	range	physical range	REZ	f_s	I/O
$V_{a,b,c}$	± 10 V	± 1000 V	0.49 V	10 kHz	AI
$I_{a,b,c}$	± 10 V	± 1000 A	30.5 mA	10 kHz	AI
$S_{a,b,c}$	5V-TTL	non-inverting	50 ns	20 MHz	DO

This process is not without limitations and problems that need to be somehow formalized and highlighted: The circuit partition and speed correspondence, resulting in a corresponding level of accuracy and stability margin of the platform [14]–[16].

The case we want to validate is the one already widely discussed in [17], but now developed to offer a benchmark to highlight the salient aspects of the implementation. On the one hand we would like to verify the performance of the control, but on the other hand we also expect to reveal the problems of the theoretical algorithm of continuous control in the practical implementation and then to improve the algorithm based on the evidence provided by the simulation C-HIL. First of all, the implementation of the C-HIL system will be presented, and then it will be expanded in the implementation and simulation aspects. The DER integration study is discussed in Section III, in order to clarify the context in which we move. Finally, the conclusion is reported in Section IV.

II. REAL-TIME C-HIL DESIGN

In this chapter, we will demonstrate how we build the RT simulation to verify the approach and how to transform it to the C-HIL. On one hand, it will verify the effectiveness of the approach; on the other hand, the C-HIL test will demonstrate the predictable undesired phenomena in practical implementation. The construction of the C-HIL system follows the structure shown in Fig. 1, incorporating a Real Time Simulator (RTS), the chosen ES and their respective graphical user interface (GUI) systems. The aim of studying grid-tied converter control makes the RTS a digital microgrid emulator including all the electrical equipment and control algorithms except for the one to be tested. The chosen ES therefore takes the responsibility of executing control codes while seeing the RTS as a microgrid. The ES and the RTS communicate with each other by their analog and digital peripherals: the controlled variables are delivered by analog-digital converters and the pulses for converter control are transmitted through digital terminals. The GUI at the controller side provides on-the-fly tuning of control parameters and supervision of intermediate variables while the GUI at the microgrid side enables arbitrary test conditions and real-time observation of grid status. As illustrated in Fig. 1, both the ES and RTS feature a sandwich structure: with the control code or microgrid model as a core and reaching for peripherals via input and output software. For one thing, this guarantees solid communication, and for another, it creates software modeling of the interface in reality, as in this case the sensors, filters and conditioning circuits.

The signal lists of RTS and ES are shown respectively in TABLE 1 and 2 which keep the consistency and viability of signal-interfacing. The interfacing signals are the voltages $V_{a,b,c}$ and currents $I_{a,b,c}$ at the point of common coupling (PCC) and the control pulses for 3-phase bridge grid-tied converter $S_{a,b,c}$. In order to deceive the ES into thinking it is functioning in a real microgrid, the analog voltage and current signals amplified by the RTS must not have lower resolution, as indicated in the tables. At the same time, they must be results iterated theoretically at least twice as fast as the sampling rate of the ES. Since the minimum two times is a result of scaling and shifting, five to ten times' solution is suggested in practice [18]. In our case, the solution of five times is taken. Even though the control is executed at 10 kHz, which is common in industry, the PWM pulses are generated by a slave processor with a time resolution of 50 ns to ensure delicate converter control. Trying to behave as real microgrid, the RTS must catch every moment of change of the pulses and thus oversampling is required and here it is 50 MHz.

Finally, knowledge of the two digital devices is notable, for it contributes to the best performance and the maximum scale of the whole simulation system. The chosen RTS is based on programmable SoC which can be configured to activate up to 4 processing cores. The simulation therefore is able to run at a fundamental real-time simulation step of microsecond level and multi-rate is supported. It is equipped with 16 analog inputs and 16 analog outputs with updating rate up to 1 MHz, and 32 digital inputs with oversampling of 50 MHz and 32 digital outputs with updating rate up to 2MHz. The RTS is equipped with a machine solver and it handles the switching behavior of power electronics in matrix. The target ES is based on master powerPC and slave DSP structure. The master is equipped with 1 A/D converter (ADC) multiplexed to four channels and 4 parallel ADCs;

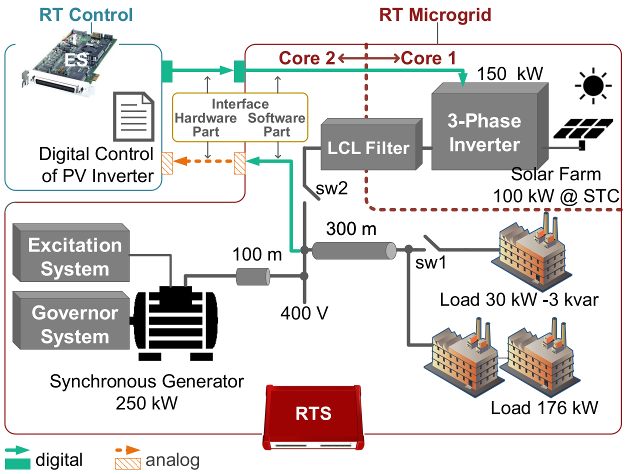

FIGURE 2. The general view of the microgrid considered. The RT control runs the algorithm of the proposed ancilary service and exchange data with the real-time simulation of the whole grid (RT microgrid). Two different real time simulator are used for the implementation.

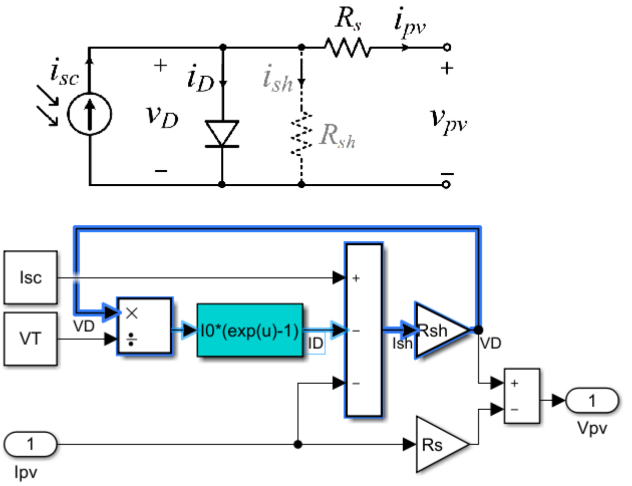

FIGURE 3. Electrical equivalent of the PV panel model and algebraic loop to be managed.

the slave is equipped with high-resolution PWM outputs. $V_{a,b,c}$ are sampled by the parallel ADCs while $I_{a,b,c}$ are sampled by the multiplexed ADCs.

A. REAL-TIME MODELING

The microgrid system is depicted in Fig. 2, composed of a 250 kW synchronous generation system, a 100 kW (under standard test condition) PV plant with a 150 kW 3-phase inverter, transmission lines of 100 m and 300 m, a fixed 176 kW load and a configurable 30 kW, −3 kvar load. The functional modules are modeled separately with input(s) and output(s) using Tustin Method and thus they can be reused in other configurations and can be coded on other RTSs as well.

1) PV ARRAY

Practical single diode model as shown in Fig. 3, which is also known as the five parameters model, is commonly used to model PV panel. However, this model results in an algebraic loop which must be solved or broken. The simple unit delay insertion causes instability, hence root-finding algorithm should be applied. Knowing the algebraic loop is an exponential equation, Lambert W function [19] can be utilized to simplify the question and then the Lambert W function will be approximated by iterative methods. Halley's method finds the root faster than Newton's method but on the other hand requires more calculation within one iteration. Even though Lambert W function together with Halley's method reduces the number of iterations, it never eliminates the iterative procedure. The unpredictable iterative action is critical in real-time simulation, especially when the PV is feeding a switching converter. Therefore, a simplified PV model is suggested by removing the shunt resistor and thus eliminating the algebraic loop, showing a compromise between the detail of model and computing capability.

The discrete model of a PV array can thus be expressed as the following equations:

$$\begin{cases} v_{pv\_array}(n) = \\ \left(v_{T\_array}(n) ln(\dfrac{i_{sc\_array}(n) - i_{pv\_array}(n-1)}{i_{0\_array}(n)} + 1) \right. \\ \left. - \dfrac{N_{ser}}{N_{par}} R_s i_{pv\_array}(n-1) \right) \\ i_{0\_array}(n) = \dfrac{N_{par} i_{sc\_module}(n)}{e^{\left(v_{oc\_module}(n)/v_{T\_module}(n)\right)} - 1} \\ i_{sc\_module}(n) = \dfrac{G(n)}{G^{STC}} \left(I^{STC}_{sc\_module} + \mu_{sc}(T(n) - T^{STC})\right) \\ i_{sc\_array}(n) = i_{sc\_module}(n) N_{par} \\ v_{oc\_module}(n) = V^{STC}_{oc\_module} + \mu_{oc}(T(n) - T^{STC}) \\ v_{T\_module}(n) = \dfrac{AkT(n)N_{cell}}{q} \\ v_{T\_array}(n) = v_{T\_module}(n) N_{ser} \end{cases} \tag{1}$$

where G, T, i_{pv_array} and v_{pv_array} are the three inputs and one output of the model: irradiance, temperature, output current with unit delay and output voltage of the PV array; $I^{STC}_{sc\_module}$ and $V^{STC}_{oc\_module}$ are the short-circuit current and the open-circuit voltage of the PV module tested under standard test condition (STC), i.e. under G^{STC} and T^{STC}; A is the diode ideality factor and N_{cell} is the number of cells that construct one module; R_s is the equivalent output series resistance of the module; μ_{sc} and μ_{oc} are the temperature drift coefficients of the short-circuit current and the open-circuit voltage tested in the unit of module; N_{ser} and N_{par} show the number of modules in a string and the number of strings in an array; k is Boltzmann constant and q is electron charge; v_T and i_0 represent thermal voltage and diode saturation current.

2) 3-PHASE INVERTER

The output of the PV array is connected to a voltage source converter (VSC) with stabilizing capacitor as shown in Fig. 4. Therefore, the PV output current i_{pv} and DC side voltage v_{DC}

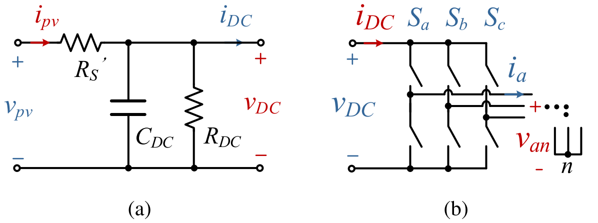

FIGURE 4. **3-phase inverter: (a) DC side capacitor (b) Voltage source converter.**

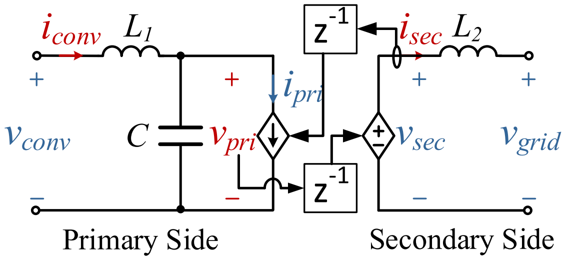

FIGURE 5. **Circuit equivalent of the partitioned LCL filter used in the real-time simulation.**

can be calculated from DC side current i_{DC} and PV output voltage v_{pv}:

$$\begin{cases} \begin{bmatrix} i_{pv}(z) \\ v_{DC}(z) \end{bmatrix} = \dfrac{1}{y_0 + y_1 z^{-1}} \begin{bmatrix} a_0 + a_1 z^{-1} & b_0 + b_1 z^{-1} \\ c_0 + c_1 z^{-1} & d_0 + d_1 z^{-1} \end{bmatrix} \begin{bmatrix} v_{pv}(z) \\ i_{DC}(z) \end{bmatrix} \\ y_0 = R_s' + R_{DC} + \dfrac{2R_s' R_{DC} C_{DC}}{T_s} \\ y_1 = R_s' + R_{DC} - \dfrac{2R_s' R_{DC} C_{DC}}{T_s} \\ a_0 = 1 + \dfrac{2R_{DC} C_{DC}}{T_s} \\ a_1 = 1 - \dfrac{2R_{DC} C_{DC}}{T_s} \\ b_0 = b_1 = c_0 = c_1 = R_{DC} \\ d_0 = d_1 = -R_s' R_{DC} \end{cases} \tag{2}$$

where C_{DC} and R_{DC} are the DC link components; R_s' is a tiny series resistance to avoid topological conflict; T_s is the sampling time.

As for the inverter, the relationship can be described according to the switching behavior:

$$\begin{cases} \begin{bmatrix} v_{an}(n) \\ v_{bn}(n) \\ v_{cn}(n) \end{bmatrix} = \dfrac{v_{DC}(n)}{3} \begin{bmatrix} 2 & -1 & -1 \\ -1 & 2 & -1 \\ -1 & -1 & 2 \end{bmatrix} \begin{bmatrix} S_a(n) \\ S_b(n) \\ S_c(n) \end{bmatrix} \\ i_{DC}(n) = \begin{bmatrix} S_a(n) & S_b(n) & S_c(n) \end{bmatrix} \begin{bmatrix} i_a(n) \\ i_b(n) \\ i_c(n) \end{bmatrix} \end{cases} \tag{3}$$

where $v_{an,bn,cn}$ are phase voltages and $i_{a,b,c}$ are phase currents at AC side; $S_{a,b,c}$ represent the controlled status of the 3-phase bridge: $S = 1$ means the upper switch is on while $S = 0$ indicates the lower switch is on.

3) LCL FILTER

The grid-tied converter is coupled to the grid through LCL filter. However, due to hardware resource restriction, the model is partitioned into two parts exactly at this filter. For clarity, a single phase model is given in Fig. 5 to demonstrate discrete modeling method omitting resistive components. The primary circuit incorporates a converter side inductor L_1 and a shunt capacitor C and it is ended by a controlled current source which replicates the secondary side current but with one step delay. The secondary side circuit is supplied by a controlled voltage source which amplifies the output voltage of the primary side with one step delay and connect to the grid through a grid side inductor L_2. Therefore the discrete model of the partitioned LCL filter can be expressed as:

$$\begin{cases} \begin{bmatrix} v_{pri}(z) \\ i_{conv}(z) \end{bmatrix} = \dfrac{1}{\sum\limits_{i=0}^{2} y_i z^{-i}} \begin{bmatrix} \sum\limits_{i=0}^{2} a_i z^{-i} & \sum\limits_{i=0}^{2} b_i z^{-i} \\ \sum\limits_{i=0}^{2} c_i z^{-i} & \sum\limits_{i=0}^{2} d_i z^{-i} \end{bmatrix} \begin{bmatrix} v_{conv}(z) \\ i_{pri}(z) \end{bmatrix} \\ i_{sec}(z) = \dfrac{1 + z^{-1}}{\frac{2L_2}{T_s}(1 - z^{-1})} \big(v_{sec}(z) - v_{grid}(z)\big) \\ v_{sec}(z) = z^{-1} v_{pri}(z) \\ i_{pri}(z) = z^{-1} i_{sec}(z) \\ [y_0 \quad y_1 \quad y_2] = [1 + \dfrac{4L_1C}{T_s^2} \quad 2(1 - \dfrac{4L_1C}{T_s^2}) \quad 1 + \dfrac{4L_1C}{T_s^2}] \\ [a_0 \quad a_1 \quad a_2] = [d_0 \quad d_1 \quad d_2] = [1 \quad 2 \quad 1] \\ [b_0 \quad b_1 \quad b_2] = [-\dfrac{2L_1}{T_s} \quad 0 \quad \dfrac{2L_1}{T_s}] \\ [c_0 \quad c_1 \quad c_2] = [-\dfrac{2C}{T_s} \quad 0 \quad \dfrac{2C}{T_s}] \end{cases} \tag{4}$$

where v_{conv} and i_{conv} are the output voltage and current of the converter; v_{pri}, i_{pri}, v_{sec} and i_{sec} are the voltages and currents at the primary side and the secondary side of the circuit partitioner; v_{grid} is the voltage of the coupling point.

4) TRANSMISSION LINES AND LOADS

Transmission lines are modeled according to $R - L$ structure. Assuming the loads are resistive and inductive-resistive, the real-time modeling of load and transmission line can be combined. Therefore, the current flowing through an inductive-resistive component symbolized as R_l and L_l can be obtained by:

$$i_l(z) = \frac{1 + z^{-1}}{(1 + \frac{2L_l}{T_s R_l}) + (1 - \frac{2L_l}{T_s R_l}) z^{-1}} \big(v_{node1}(z) - v_{node2}(z)\big) \tag{5}$$

where v_{node1} and v_{node2} are the two nodes joined by the component; i_l is the current flowing from node1 to node2. If it is a load, $V_{node2} = 0$.

B. OTHER REAL-TIME ISSUES

The RTS differentiates the real-time simulation from offline simulation in the limit hardware resources, i.e. computing power [20]. So in the following paragraphs, we will discuss the realization of the simulated system from circuit partition and multi-rate aspects which are significant approaches to use the RTS to the fullest.

1) CIRCUIT PARTITION

As it is depicted in Fig. 6 (a), the microgrid system can be seen as a six-node power system with switching devices. Since the total computing load is contributed by both nodal equations and update of state variables, the number of nodes and the sizes of admittance matrices of subsystems are detrimental [21]. However, the switching devices enforce repeat calculation under different switching statuses of all related matrices by 2^{w_s} times, where w_s is the weight of the switch. In order to reduce calculations or to reduce the size of the whole matrix, less nodes and state variables are promoted to connect to the switches. Fig. 6 (b) is a graphical description of computing load before partitioning, including nodal equations and state variables history update. Each calculation point has its own size of matrix, which can be expressed as weight w_i $(i = 1, \ldots, 16)$. Because of the existence of inverter (3 pairs of half-bridge), configurable load (sw1 in Fig. 2) and PV Plant connection switch (sw2 in Fig. 2), the amount of calculation is $C_{core1} = 2^{(3+1+1)} \cdot \sum_{i=1}^{16} w_i$. It indicates that the matrix of the whole system is giant because of the 32 replicas of the 16 groups of variables. Therefore, an ideal transformer model (ITM) has been adopted to decouple the circuit into two sub-circuits and the method has been shown in Fig. 5. The ITM is placed inside the LCL output filter of the PV plant, more specifically, between the capacitor C and the inductor L_2 with the controlled current source feeding back the PV generation and the controlled voltage source interfacing to the grid. This ITM amplifies the voltages of C and supplies them to L_2 terminal; at the same time, it senses the currents of L_2 and feeds them back to C terminal. The computing burden after partitioning is shown in Fig. 6 (c) with the 3-phase inverter in one computing unit involving far less calculation points: $C'_{core1} = 2^3 \cdot \sum_{i=13}^{16} w_i$ and the rest even though with many calculation points but few switches: $C'_{core2} = 2^{(1+1)} \cdot \sum_{i=1}^{13} w_i$. As a result, the partitioned computing loads of the two sub-circuits are 25% and 3% instead of 145% from one complete circuit, guaranteeing viable utilization of RTS and permitting expansion of the microgrid scale.

This placement of ITM is based on a comprehensive consideration of not only hardware resource occupancy, but also accuracy, stability and variable coherence [22]–[25]. Firstly, the LCL filter ensures accuracy by limiting the frequency of the entering signals. This is because that the ITM is achieved digitally with one-step command delay and one-step feedback delay, and thus it is sensitive to the high frequency stimulus. Secondly, knowing that the PV plant connects to a microgrid composed of transmission lines, loads and a synchronous generator, the voltage-amplified ITM brings larger stability margin by being placed closer to the stimulus. And finally, this placement does not cause topological conflicts and therefore, no auxiliary circuits, which distort the simulation results, are required to guarantee variable coherence.

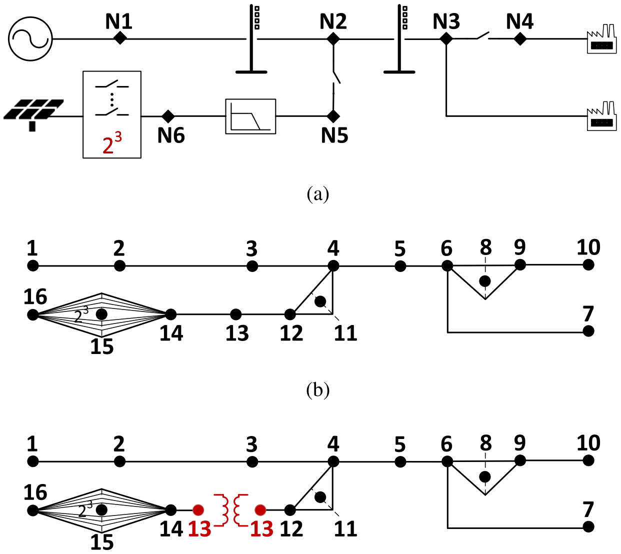

(a)

(b)

(c)

FIGURE 6. **Graphical description of computing load. (a) The 6-node system. (b) Computing load before partitioning. (c) Computing load after partitioning.**

2) MULTI-RATE SYSTEM

The system has been designed as multi-rate. Not only does it balance computing burden and simulation performance, it also plays an important role in reliable interfacing. The fundamental simulation step is set as 1 μs and most nodes and state variables are calculated or updated at this rate. Due to the slow dynamic characteristics, the synchronous generation has been assigned a 5 kHz rate. The multi-rate assignment around the interface is shown in Fig. 7 (a). At the real-time control side, sampling, control algorithm and carrier frequency are all set to 10 kHz which is common in electrical system and furthermore, the 20 MHz PWM generation helps produce fine pulses with resolution of 0.05 %. At the real-time model side, the pulses are sampled at 50 MHz with high accuracy. Finally, the pulses are delivered to the inverter at 1 MHz. We can infer from the above information that the controlled variables, i.e. the voltages and currents at the coupling point, must contain components of the 10 kHz switching frequency. Therefore, these variables are firstly sampled internally

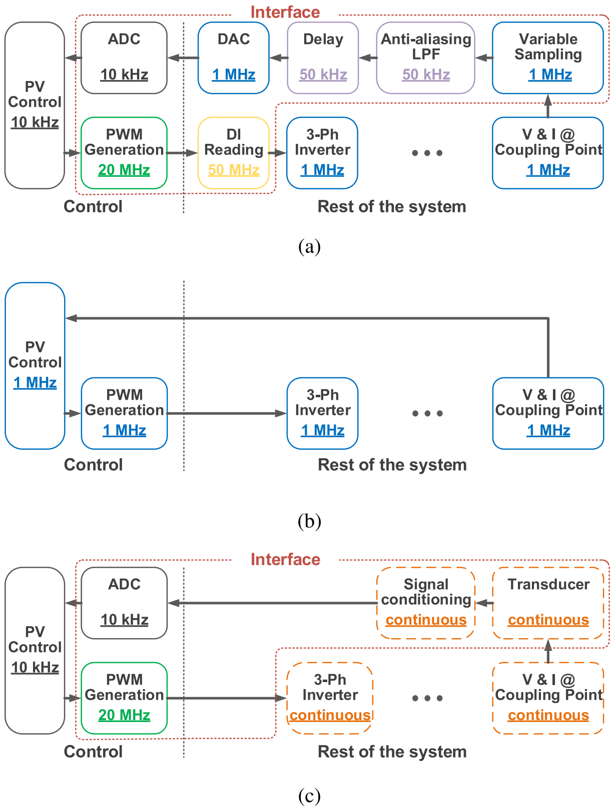

FIGURE 7. Interfacing method and execution rates (underlined). (a) C-HIL simulation. (b) Offline simulation. (c) Field test.

at 1 MHz, and then filtered with the cut-off frequency of 2 kHz executed at 50 kHz. Delays are added to emulate the real signal transmission. Finally, the signals are amplified by the DACs. By emulating the limit bandwidth of the sensors and conditioning circuit, the aliasing issues are also eliminated.

III. DER INTEGRATION STUDY ON C-HIL

A novel ancillary service has been proposed previously in [17] to help recover frequency transients. The approach leverages the reactive power by controlling the grid-tied converters when the distributed generation is not working under the full power rating and thus it does not require additional reserves. Therefore, it is appropriate for established power systems to further improve frequency transients and at the same time increases utilization of the installed equipment. We use a PV to exploit some properties it has, including that of not needing to adjust the frequency of a rotating mass, as in the case of wind turbines, while it can be easily replicated with storage systems. In the first case the algorithms are more complex and in literature there are some examples [26], while in the case of the battery storage system the algorithm used can be the same, with the advantage to work also in charging phase In order to slow down the frequency change during a step load transient, the electromagnetic torque must be stabilized. The electromagnetic torque is a comprehensive result of armature voltage, electromotive force and their electric angle. Traditional frequency-regulation ancillary services compensate directly the variation of the active power and thus slow down the change of electric angle, gaining time for the prime mover. The proposed approach, however, influences the armature voltage by injecting / absorbing reactive power to / from the grid.

In the context of the predefined microgrid, this ancillary service is integrated into the PV control strategy, as it is shown in Fig. 8. The measurement and Phase Locked Loop (PLL) blocks sample the PCC information and transform it into d,q-axis components, thus frequency, d,q voltages and currents, and phase angle are all available for the the control loop. According to the measured ambient conditions, the maximum active power generation is firstly estimated. At the same time, a reactive power reference for the control loop is generated by the deviation of frequency apart from the reference, achieving a reactive power control where the current references in d,q axis can be calculated knowing the power and voltage estimation. In the inner current close-loop, PI control is applied.

A. C-HIL TEST OF ANCILLARY SERVICE

In order to check its feasibility in practical implementation, the ancillary service has been tested on the C-HIL microgrid simulation platform. The ancillary service has proved effective on damping frequency overshooting by C-HIL simulation with the results shown in Fig. 9, reducing the frequency overshooting by 12.5 % and damping the rate of change of frequency (ROCOF). But at the same time, it slows down the recovery of the voltage transients as expected before.

However in the observation of intermediate variables, a bias of reactive power is detected at the microgrid model side as it is shown in Fig. 10. This incorrect recognition of reactive power by the ES induces undesirable reactive power flow and probably leads to performance abatement of the ancillary service. In steady state, where the reactive power should be zero, a significant amount of reactive power has been found flowing through the PV system without being noticed by its control system, reaching about 6% of its nominal generation. Therefore, in the following subsections, studies are made to understand the phenomenon and to improve the algorithm in practice.

B. VARIABLE TRANSMISSION

The ancillary service was proposed under the assumption that the transmission of controlled variables had infinite bandwidth, unit gain and zero latency. Therefore, we firstly start from the analysis of the variable transmission chain. Fig. 7 has illustrated the variable transmission processes with execution rates underlined in C-HIL, in offline simulation and in field test respectively. The field test consists of a digital ES and an analog electrical system. C-HIL is able to use the same ES but has to generate the continuous variables and to emulate the analog devices out of necessity for interface, in a digital way. Several aspects make C-HIL simulation approximate to field test: 1) The microgrid is simulated at a fundamental

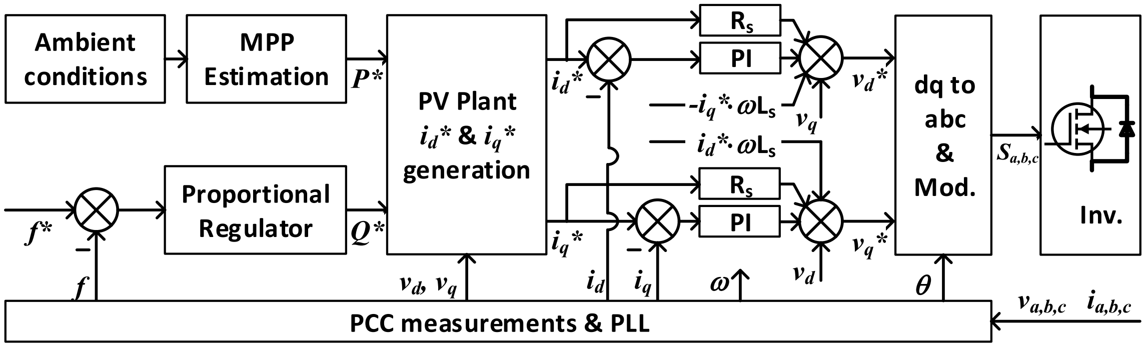

FIGURE 8. Ancillary service implemented in PV system.

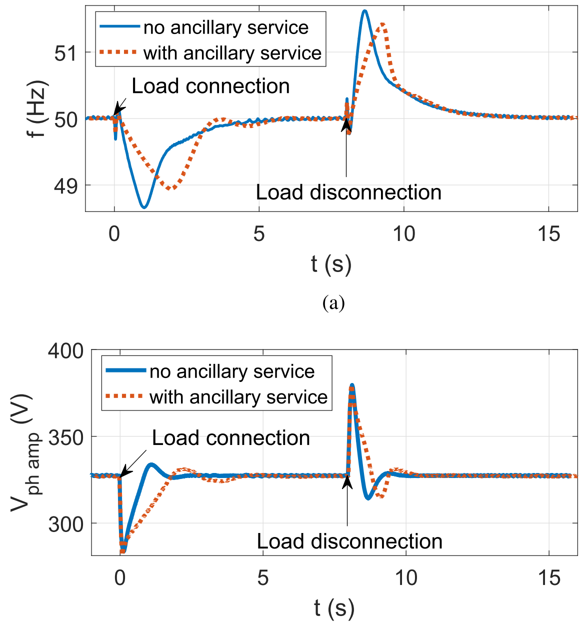

FIGURE 9. Performance of ancillary service during transients. (a) Improvement on frequency transients. (b) Influence on voltage transients.

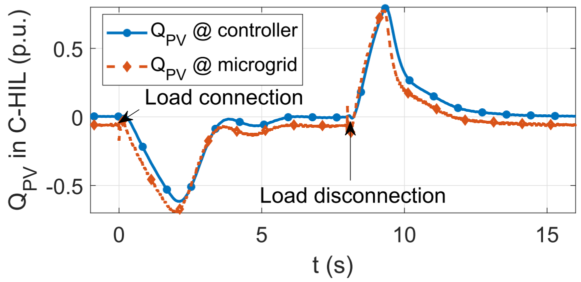

FIGURE 10. C-HIL PV reactive power seen by the controller (blue) and seen by the microgrid (orange).

rate of 1 MHz, which is a sufficient approximation to reality; 2) The 50 MHz oversampling at the control command receiver side does not miss any control command update; 3) The analog controlled variables update five times as fast as the control reading; 4) Neglecting the accuracy issues and noise, C-HIL tries to emulate the transducer and signal conditioning circuit by filtering and introducing delay, corresponding to the bandwidth of transducers and operational amplifiers and their response time. Offline simulation, on the contrary, programs the whole system digitally for theoretical proof, hence in the absence of interface, only the ideal system is usually considered, in other words, the controlled variables are delivered to the control under 1 MHz bandwidth, unit gain and zero latency. Moreover, the offline test's 1 MHz variable reading, algorithm execution and command update break the natural frequency barrier set by the digital processor. Without thorough consideration of features of ES and interface, offline simulation may provide results that cannot be replicated in reality.

By and large, C-HIL simulation is closer to field test than offline simulation is, due to the inclusion of real ES and the awareness of the interface. So, the incorrect recognition of reactive power may be because of the ideal-condition-based ancillary service.

C. ANCILLARY SERVICE IMPROVEMENT

Since the ancillary service is implemented in d-q coordinate, a phase locked loop (PLL) is used to synchronize voltages at the coupling point. The obtained phase angle is then applied in Park Transformation of PV output currents and in Inverse Park Transformation of modulation wave. So, the accuracy of the phase angle differential between the voltages and currents determines the accuracy of the transformed currents in the d-q coordinate set by the voltages. The transformed voltages and currents are the feedback of control loop and the elements used to calculate the power. Therefore, in the digital realization of the algorithm, it is necessary to correct the phase angle according to the knowledge of variable transmission.

As the mapping of variable transmission shown in Fig. 7 (a) has indicated, the non-ideal sections are anti-aliasing filter, response delay and quantization process. The induced distortion of variables is mainly reflected on absolute time delay and phase delay. For the fundamental wave is

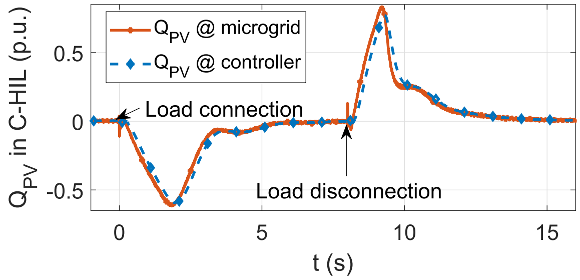

FIGURE 11. C-HIL PV reactive power seen by the controller (blue) and seen by the microgrid (orange) after modifying the ancillary service.

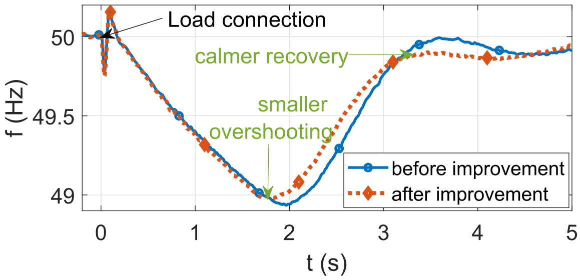

FIGURE 12. Improvement on frequency transients after modifying the ancillary service (orange).

essential to the control, we focus only on the 50 Hz component and thus we are able to transform phase delay to time delay. The transducers are tested experimentally under the nominal voltage and current level of the PV plant and the delay of the 50 Hz components are recorded as t_{VT} for voltage transducer and t_{CT} for current transducer. The anti-aliasing filter is designed as a set of 1^{st} order low pass filters in z-domain. Based on the derived phase delay, the delay time of the 50 Hz component can be obtained as t_{LPF_V} and t_{LPF_I}. In our C-HIL experiment, 3-phase voltages are sampled by parallel ADCs ($t_{conversion} = 800$ ns) while 3-phase currents are sampled by multiplexed ADCs ($t_{conversion} = 2\ \mu$s) and the sampling is done every 100 μs. The time duration, from the instant when the analog signals are ready to the moment at which the controller obtained the quantified values, can be roughly estimated and recorded as $t_{sampling\_V}$ and $t_{sampling\_I}$. Different execution sequences result in different $t_{sampling\_I,V}$. Obviously, arranging the voltage sampling just ahead of the current sampling in the program will lead to the least time shift between voltage and current variables. Besides, the round-off action in the quantization process introduces time delay as well. Taking the mean value as the approximation, the time delay can be estimated as half the sampling period, i.e. $t_{quantization} = 50\ \mu$s. Therefore, the time delays of the voltages and currents can be estimated as:

$$t_{delay\_V} = t_{VT} + t_{LPF\_V} + t_{sampling\_V} + t_{quantization} \quad (6)$$

$$t_{delay\_I} = t_{CT} + t_{LPF\_I} + t_{sampling\_I} + t_{quantization} \quad (7)$$

The phase angle differential between the voltages and currents are thus obtained. Before the Park Transformation of the currents, the phase angle can be corrected by compensating the differential.

We have modified the ancillary service with phase angle compensation and have tested it again on the C-HIL platform. After integrating the non-ideal variable transmission features to the algorithm, the reactive power seen by the controller overlaps well the one flowing in the microgrid (Fig. 11), except for the time delay at fast transients caused by the filtering actions in the control algorithm. In addition, the frequency overshooting is further reduced and the recovery oscillation is damped with the help of the correction, as represented in Fig. 12.

IV. CONCLUSION

In this article we have shown the development of a microgrid co-simulation platform using the C-HIL technique, which aims to study the integration of DER. The real-time implementation of the microgrid was discussed starting from aspects of real-time modeling, circuit partitioning and multirate system design. The proposed methodology was used to study an auxiliary service. With the help of C-HIL simulation, the intrinsic contributors to the problems studied were identified and the corresponding modification to the ancillary service was proposed and proved effective. The proposed methodology offers an original starting point for study, for all those who want to approach the problem of the study of micro-nets in a context of RTS simulation.

REFERENCES

[1] M. Prodanovic and T. C. Green, "High-quality power generation through distributed control of a power park microgrid," *IEEE Trans. Ind. Electron.*, vol. 53, no. 5, pp. 1471–1482, Oct. 2006.

[2] J. Liu, Y. Miura, and T. Ise, "Comparison of dynamic characteristics between virtual synchronous generator and droop control in inverter-based distributed generators," *IEEE Trans. Power Electron.*, vol. 31, no. 5, pp. 3600–3611, May 2016.

[3] S. Barcellona, Y. Huo, R. Niu, L. Piegari, and E. Ragaini, "Control strategy of virtual synchronous generator based on virtual impedance and band-pass damping," in *Proc. Int. Symp. Power Electron., Elect. Drives, Automat. Motion (SPEEDAM)*, Jun. 2016, pp. 1354–1362.

[4] G. De Zotti, S. A. Pourmousavi, H. Madsen, and N. K. Poulsen, "Ancillary services 4.0: A top-to-bottom control-based approach for solving ancillary services problems in smart grids," *IEEE Access*, vol. 6, pp. 11694–11706, 2018.

[5] Z. Li, C. Zang, P. Zeng, H. Yu, S. Li, and J. Bian, "Control of a grid-forming inverter based on sliding-mode and mixed H_2/H_∞ control," *IEEE Trans. Ind. Electron.*, vol. 64, no. 5, pp. 3862–3872, May 2017.

[6] M. N. Alam, S. Chakrabarti, and A. Ghosh, "Networked microgrids: State-of-the-art and future perspectives," *IEEE Trans. Ind. Informat.*, vol. 15, no. 3, pp. 1238–1250, Mar. 2019.

[7] A. S. Vijay, S. Doolla, and M. C. Chandorkar, "Real-time testing approaches for microgrids," *IEEE J. Emerg. Sel. Topics Power Electron.*, vol. 5, no. 3, pp. 1356–1376, Sep. 2017.

[8] M. D. O. Faruque *et al.*, "Real-time simulation technologies for power systems design, testing, and analysis," *IEEE Power Energy Technol. Syst. J.*, vol. 2, no. 2, pp. 63–73, Jun. 2015.

[9] J. Wang, Y. Song, W. Li, J. Guo, and A. Monti, "Development of a universal platform for hardware in-the-loop testing of microgrids," *IEEE Trans. Ind. Informat.*, vol. 10, no. 4, pp. 2154–2165, Nov. 2014.

[10] F. Mahmood, L. Vanfretti, M. Pignati, H. Hooshyar, F. Sossan, and M. Paol, "Experimental validation of a steady state model synthesis method for a three-phase unbalanced active distribution network feeder," *IEEE Access*, vol. 6, pp. 4042–4053, 2018.

[11] A. Spina, R. Palaniappan, D. Hilbrich, U. Häger, and C. Rehtanz, "Comparison between CHIL simulation and hardware test of a dynamic power flow controller," in *Proc. IEEE Manchester PowerTech*, Jun. 2017, pp. 1–6.

[12] R. Morello, R. Di Rienzo, R. Roncella, R. Saletti, and F. Baronti, "Hardware-in-the-loop platform for assessing battery state estimators in electric vehicles," *IEEE Access*, vol. 6, pp. 68210–68220, 2018.

[13] Y. Huo, G. Gruosso, and L. Piegari, "Power hardware in the loop simulator of photovoltaic plant for smart grid interation analysis," in *Proc. IEEE Int. Conf. Environ. Elect. Eng. IEEE Ind. Commercial Power Syst. Eur. (EEEIC/I&CPS Europe)*, Jun. 2017, pp. 1–5.

[14] F. Lehfuß, G. Lauss, and T. Strasser, "Implementation of a multi-rating interface for Power-Hardware-in-the-Loop simulations," in *Proc. 38th Annu. Conf. IEEE Ind. Electron. Soc. (IECON)*, Oct. 2012, pp. 4777–4782.

[15] I. D. Yoo and A. M. Gole, "Compensating for interface equipment limitations to improve simulation accuracy of real-time power hardware in loop simulation," *IEEE Trans. Power Del.*, vol. 27, no. 3, pp. 1284–1291, Jul. 2012.

[16] A. Castro, P. Zuniga, F. A. Uribe, and E. Barocio, "Phase compensation scheme to improve the accuracy of a power hardware-in-the-loop experiment based on a synchronous generator," in *Proc. IEEE Eindhoven PowerTech*, Jun. 2015, pp. 1–6.

[17] Y. Huo, S. Barcellona, G. Gruosso, and L. Piegari, "Definition and analysis of an innovative ancillary service for microgrid stability improvement," in *Proc. Int. Symp. Power Electron., Elect. Drives, Automat. Motion (SPEEDAM)*, Jun. 2018, pp. 990–995.

[18] G. D'Antona and A. Ferrero, *Digital Signal Processing for Measurement Systems: Theory and Applications*. New York, NY, USA: Springer, 2006.

[19] R. M. Corless, G. H. Gonnet, D. E. G. Hare, D. J. Jeffrey, and D. E. Knuth, "On the LambertW function," *Adv. Comput. Math.*, vol. 5, pp. 329–359, Dec. 1996. doi: 10.1007/BF02124750.

[20] D. Paul, R. Achar, M. S. Nakhla, and N. M. Nakhla, "Addressing partitioning issues in parallel circuit simulation," *IEEE Trans. Very Large Scale Integr. (VLSI) Syst.*, vol. 22, no. 12, pp. 2713–2723, Dec. 2014.

[21] P. Zhang, J. Marti, and H. W. Dommel, "Network partitioning for real-time power system simulation," in *Proc. Int. Conf. Power Syst. Simulation (IPST05)*, Jun. 2005, pp. 1–6.

[22] W. Ren *et al.*, "Interfacing issues in real-time digital simulators," *IEEE Trans. Power Del.*, vol. 26, no. 2, pp. 1221–1230, Apr. 2011.

[23] W. Ren, M. Steurer, and T. L. Baldwin, "Improve the stability and the accuracy of power hardware-in-the-loop simulation by selecting appropriate interface algorithms," *IEEE Trans. Ind. Appl.*, vol. 44, no. 4, pp. 1286–1294, Jul./Aug. 2008.

[24] W. Ren, M. Steurer, and T. L. Baldwin, "An effective method for evaluating the accuracy of power hardware-in-the-loop simulations," *IEEE Trans. Ind. Appl.*, vol. 45, no. 4, pp. 1484–1490, Jul. 2009.

[25] B.-I. Crăciun *et al.*, "Grid integration of PV power based on PHIL testing using different interface algorithms," in *Proc. 39th Annu. Conf. IEEE Ind. Electron. Soc.*, Nov. 2013, pp. 5380–5385.

[26] H. Badihi, Y. Zhang, and H. Hong, "Active power control design for supporting grid frequency regulation in wind farms," *Annu. Rev. Control*, vol. 40, pp. 70–81, 2015.

YUJIA HUO (S'17) received the B.Sc. degree in electrical engineering (EE) from Xi'an Jiaotong University, Xi'an, China, in 2012, and the double M.Sc. degrees in EE from Xi'an Jiaotong University and the Politecnico di Milano, Italy, in 2015. She is currently pursuing the Ph.D. degree in EE with the Politecnico di Milano. Her research interests include hardware-in-the-loop simulation, microgrid, and control techniques for power electronics devices.

GIAMBATTISTA GRUOSSO (M'01–SM'12) was born in 1973. He received the M.S. and Ph.D. degrees in electrical engineering from the Politecnico di Torino, Italy, in 1999 and 2003, respectively. From 2002 to 2011, he was an Assistant Professor with the Department of Electronics and Informatics, Politecnico di Milano, where he has been an Associate Professor, since 2011. His current research interests include electrical vehicles transportation electrification electrical power systems optimization, and simulation of electrical systems. He has authored more than 80 papers on Journals and conferences on the topic.

• • •